# Fast simulators for satellite cloud optical centroid pressure retrievals, 1. Evaluation of OMI cloud retrievals

**J. Joiner[1], A. P. Vasilkov[2], Pawan Gupta[3,7], P. K. Bhartia[1], Pepijn Veefkind[4], Maarten Sneep[4], Johan de Haan[4], Igor Polonsky[5], and Robert Spurr[6]**

[1]Goddard Space Flight Center, Laboratory for Atmospheres, Greenbelt, MD, USA
[3]University of Maryland, Baltimore County, Baltimore, MD, USA
[4]Royal Dutch Meteorological Institute (KNMI), de Bilt, Netherlands
[5]Colorado State University, Ft. Collins, CO, USA
[6]RTSolutions, Cambridge, MA, USA
[7]Universities Space Research Association, Columbia, MD, USA

Correspondence to: Joanna Joiner (Joanna.Joiner@nasa.gov)

## Abstract

## 1 Introduction

Information about the abundances of many chemically- and radiatively-active trace gases is retrieved using satellite solar backscatter instruments that make measurements at near-infrared (NIR) through ultraviolet wavelengths. These trace-gas retrieval algorithms commonly require information about the mean photon path length in the atmosphere to properly account for the presence of clouds and aerosol. One way to express photon path length information is the so-called cloud optical centroid pressure (also known as the effective cloud pressure), or cloud OCP, that is defined as the characteristic pressure of a single cloud layer within the context of a particular cloud model. The use of the word "optical" in OCP is designed to distinguish it from the common mass centroid. In this paper, we provide a simple method for estimating this quantity using a pressure-weighting scheme where the weights depend upon optical parameters of clouds and/or aerosol.

Several different algorithms make use of cloud OCPs to accurately retrieve information about $O_3$ including estimates of the total column (e.g., Coldewey-Egbers et al., 2005; Roozendael et al., 2006; Veefkind et al., 2006) and tropospheric concentrations (e.g., Ziemke et al., 2009; Joiner et al., 2009). Other studies have focused on various aspects of cloud-related errors on $O_3$ retrievals (e.g., Koelemeijer et al., 1999; Vasilkov et al., 2004; Kokhanovsky et al., 2007b; Joiner et al., 2006).

Cloud OCPs have also been used in other trace-gas retrievals such as those for $NO_2$ (e.g., Bucsela et al., 2006) and $CO_2$ (e.g., Reuter et al., 2010). In addition, cloud OCPs have been used for other applications such as short-wave flux calculations (Joiner et al., 2009; Vasilkov et al., 2009) and detection of multi-layer clouds (Joiner et al., 2010).

The instruments used in these studies include the Global Ozone Monitoring Experiments (GOME and GOME-2) (Burrows et al., 1999). The first GOME flew on the European Space Agency's (ESA's) European Remote Sensing 2 (ERS-2) launched in 1995. GOME-2 instruments are currently flying on the European Meteorological

Satellite Operational (EuMetSat's MetOp) series of satellites. Similar to the GOME instruments, the SCanning Imaging Absorption SpectroMeter for Atmospheric CHartographY (SCIAMACHY) (Bovensmann et al., 1999) on ESA's Environmental Satellite (EnviSat) launched in 2002, makes spectral measurements from UV to NIR wavelengths. In addition, the Ozone Monitoring Instrument (OMI) (Levelt et al., 2006), flying on the (U.S.) National Aeronautics and Space Administration's (NASA's) Aura satellite since 2004, measures backscattered spectra in the UV and visible.

There are several different remote sensing techniques that have been used to retrieve cloud OCPs or similar information about cloud vertical structure. These include rotational-Raman scattering in the ultraviolet (UV) (Joiner and Bhartia , 1995; Joiner et al., 2004), oxygen dimer ($O_2$-$O_2$) absorption near 477 nm (Acarreta et al., 2004; Sneep et al., 2008), and absorption in the $O_2$-A band near 760 nm (e.g., Koelemeijer et al., 2001, 2002; Vanbauce et al., 2003; Kokanovsky et al., 2006). The $O_2$-A band has also been used to retrieve information about aerosol plume height (e.g., Dubuisson et al., 2009).

Cloud OCP errors have been calculated from retrieval theory and radiative transfer calculations (e.g., Koelemeijer et al., 2001; Acarreta et al., 2004; Daniel et al., 2003; Vasilkov et al., 2008). Several other studies have evaluated various satellite cloud OCP retrievals. Sneep et al. (2008) intercompared three different cloud OCP data sets from the A-train constellation of satellites. In another evaluation approach, Vasilkov et al. (2008) compared cloud OCPs with collocated data from the CloudSat radar and the Aqua MODerate-resolution Imaging Spectrometer (MODIS) using radiative transfer calculations. Only a few samples were compared in this study.

In this paper, we formulate fast simulators that use cloud/aerosol extinction profiles as inputs to generate estimates of cloud/aerosol OCPs. These fast OCP simulators have several potential applications. Here, we use them for further evaluation of OMI cloud OCP retrievals with CloudSat/MODIS data over a wide range of conditions. In addition, our fast cloud OCP simulators will be useful for comparisons of general circulation model cloud vertical structure with satellite-derived OCPs. Finally, fast simulators

are ideal for assimilation of satellite-derived OCPs where computational efficiency is important.

The paper is structured as follows: We describe the satellite data sets used here in Sect. 2. Sections 3 and 4 detail the formulation of full and fast OCP retrieval simulators, respectively. The fast OCP simulators are applied to CloudSat/MODIS data and compared with two OMI OCP retrievals in Sect. 5. Conclusions are given in Sect. 6.

## 2 Satellite data sets

In this work, we make use of several data sets from the so-called A-train constellation of satellites. These satellites fly in formation in polar orbits, crossing the equator within 15 minutes of each other near 01:30 local time.

### 2.1 OMI cloud OCP data sets

We examine two types of cloud OCP retrievals from OMI. OMI is a spectrometer that makes Earth and solar measurements at ultraviolet and visible wavelengths from 270-500 nm with a spectral resolution of approximately 0.5 nm (Levelt et al., 2006). Its ground footprint varies; near nadir, it is approximately 12 km along the satellite track and 24 km across the track. The footprint size increases towards the swath edge.

There are two independent approaches used to retrieve cloud OCP from OMI that are summarized in Stammes et al. (2008). These algorithms make use of the basic property that clouds shield the atmosphere below them from atmospheric scattering and absorption, thus reducing photon pathlengths. The retrievals rely upon physical effects produced by well-mixed, well-characterized atmospheric constituents, namely absorption by oxygen and scattering from both oxygen and nitrogen.

Both OMI cloud algorithms use a simplified model to account for the complex effects of clouds on observed radiances. This approach, sometimes referred to as the Mixed Lambertian Equivalent Reflectivity (MLER) model, represents an observed satellite

pixel radiance ($I_{obs}$) as a weighted combination of clear and cloudy subpixel radiances, $I_{clr}$ and $I_{cld}$, respectively, i.e.,

$$I_{obs} = I_{clr}(1 - f_{eff}) + I_{cld} f_{eff}, \quad (1)$$

(McPeters et al., 1996; Koelemeijer et al., 1999) where the weighting factor, $f_{eff}$, is known as the effective cloud fraction. The model accounts for partial cloud cover and scattering and absorption beneath thin clouds by representing the cloudy portion of the pixel, $I_{cld}$, as a Lambertian surface with a reflectivity of 0.8. Since most clouds have a reflectivity of less than 0.8, it follows that $f_{eff}$ is less than the geometrical cloud fraction $f_g$. Justifications of 0.8 as the cloud reflectivity and other details of the MLER model are given in Koelemeijer et al. (1999), Ahmad et al. (2004), and Stammes et al. (2008).

### 2.1.1 OMI $O_2$-$O_2$ product

The OMI $O_2$-$O_2$ algorithm, henceforth referred to as OMI O2-O2, makes uses of a collision-induced absorption ($O_2$-$O_2$) band at 477 nm. This is the strongest oxygen absorption feature within the OMI wavelength range. The algorithm uses the so-called Differential Optical Absorption Spectroscopy (DOAS) approach to determine a slant column amount of $O_2$-$O_2$ and continuum reflectance from OMI reflectances between 460 nm and 490 nm in OMI's visible channel. The algorithm uses a table-lookup approach to compute the effective cloud fraction and optical centroid pressure. Details of the approach are given in Acarreta et al. (2004), Sneep et al. (2008), and Stammes et al. (2008). The table lookup scheme has been modified recently by incorporating additional nodes. We use the latest available version of the algorithm here (V1.2.3.1). This version contains a new field called "CloudPressureNotclipped" in which the cloud pressures are allowed to extend beyond the surface pressure. We use this field for all cloud OCP comparisons.

### 2.1.2 OMI RRS product

The OMI rotational-Raman (RRS) algorithm makes use of the filling-in of solar Fraunhofer lines by rotational-Raman scattering (RRS) to determine the cloud OCP. It uses a wavelength not significantly affected by RRS (354.1 nm) to determine the effective cloud fraction. This algorithm uses wavelengths between 345 and 355 nm in OMI's UV-2 detector to fit the high-frequency spectral structure of the solar-normalized radiance produced by the filling-in/depletion effect of RRS as described in Joiner et al. (2004), Joiner and Vasilkov (2006), and Vasilkov et al. (2008). A wavelength shift between Earth and solar spectra is also determined. A soft-calibration approach that uses data over the Antarctic plateau corrects for artifacts in the individual detector elements that produced a so-called striping effect that was present from the beginning of the data record.

Modifications to the algorithm following the validation work of Vasilkov et al. (2008) include the use of a surface albedo climatology over land based on data from the Total Ozone Mapping Spectrometer (TOMS) (C. Ahn, private communication, 2009). The most recent version also incorporates a Cox-Munk (Cox and Munk, 1954) treatment of the ocean surface scattering based on a mean surface wind speed of 6 m/s in conjunction with a water-leaving radiance climatology again based on TOMS data. The version of the OMI RRS cloud algorithm used here is 1.8.3.

## 2.2 CloudSat/MODIS 2B TAU product

We make use of cloud extinction profile retrievals known as the CloudSat 2B-TAU product (Cloudsat, 2008). Extinction profiles are estimated using the 94 GHz CloudSat Cloud Profiling Radar (CPR) reflectivity measurements (Stephens et al., 2008) and radiances from the Aqua MODIS instrument. The native CloudSat measurements are made as a function of altitude. When comparing with OMI retrievals, we use the 2B GEOPROF data set, based on information from the European Center for Medium-range Weather Forecasts (ECMWF), to provide the 2B TAU extinction profiles as a

function of pressure. All CloudSat data sets used here are from revision 4.

### 2.3 MODIS cloud top pressure

We collocated MODIS cloud-top pressure retrievals (Menzel et al., 2008) from collection 5 with OMI pixels as described by Joiner et al. (2010). For each OMI pixel, we save the minimum, maximum, mean, and standard deviation of the cloud top pressure. This provides some information on OMI subpixel heterogeneity. It should be noted that cloud-top pressure is not always a good indicator of sub-pixel heterogeneity in the cloud OCP (Joiner et al., 2006).

## 3 Full rotational-Raman retrieval simulator ($R^3S$)

We developed a full OMI rotational-Raman retrieval simulator ($R^3S$) using radiative transfer (RT) calculations carried out with the generic linearized discrete ordinate rotational-Raman scattering code, known as LIDORT-RRS (Spurr et al., 2008). $R^3S$ was used by Vasilkov et al. (2008) to compute errors in the OMI rotational-Raman (RRS) scattering cloud OCP retrieval. It was also used to simulate cloud OCP from CloudSat/MODIS 2B-TAU extinction profiles for a few soundings in a deep convective complex. These simulations were then compared with actual OMI RRS retrievals.

As inputs for $R^3S$ in this study, we simulate satellite cloudy-sky radiances based on CloudSat 2B-TAU profiles using plane-parallel clouds with three different cloud phase functions. The first of these is the water-droplet C1 cloud model with a modified-gamma size distribution with an effective radius of 6 µm (Deirmendjian, 1969). The second is a Henyey-Greenstein (H-G) phase function with asymmetry factor $g$=0.85. Third, we use a shortwave model of ice clouds with an effective diameter of 30 µm (Baum et al., 2005). In all cases, the cloud single scattering albedo is set to unity. We found that the phase function had very little effect on the simulated cloud OCPs except for the lowest values of cloud optical thickness (generally less than 5). As our focus is for

cloud optical thicknesses typically greater than 5, all results shown here will use the C1 cloud model.

For both forward and inverse calculations Earth's surface is assumed to be Lambertian at a pressure of 1013 hPa with a reflectivity of 0.05. The value of the assumed surface reflectivity is not of great importance for the simulations in this paper as long as reasonable values are used; however, it is of critical importance that the values assumed in both forward and inverse calculations are consistent in order to prevent errors from being introduced into the simulation.

As described in Vasilkov et al. (2008), the effects of rotational-Raman scattering are simulated at a single wavelength while the effective cloud fraction is derived at a second wavelength. A simple table-lookup retrieval scheme is then performed using simulated data at those wavelengths. Data are simulated for the OMI solar and satellite viewing zenith angles corresponding to a given CloudSat location.

Next, we extend the work of Vasilkov et al. (2008) comparing $R^3S$ with OMI RRS retrievals for a full day of CloudSat 2B-Tau profiles. OMI rotational-Raman cloud pressure retrievals are not performed when the effective cloud fraction drops below 5%. This happens not only when geometrical cloud fractions are small, but also for cases when the geometrical cloud fraction may be large but the optical thickness is low, such as optically thin cirrus. Therefore, OMI effective cloud fractions must be greater than 5% for a successful collocation. To minimize the amount of computations performed in $R^3S$, we averaged the layer optical thicknesses of all CloudSat soundings falling within a given OMI pixel. This provides a single optical extinction profile for each OMI pixel. We used only profiles with total optical thickness $\tau > 5$.

As in Joiner et al. (2010), we attempt to remove situations where the averaged CloudSat profiles are not representative of the much larger OMI pixel. The nadir-viewing CloudSat has only a single field-of-view of width approximately 1.4 km across the satellite track as compared with OMI's 24 km width. Therefore, the CloudSat slice along the satellite track samples only a small fraction of an OMI pixel. Here, we eliminated pixels for which the MODIS cloud-top pressure standard deviation within the OMI pixel was

greater than 100hPa.

Figure 1 shows a comparison of the $R^3S$-generated cloud OCP based on with actual OMI RRS cloud OCP retrievals using a 2D histogram. We used 2972 CloudSat 2B-TAU profiles from 13 November 2006 for this comparison. There is generally good agreement, although OMI RRS retrievals are biased low by approximately 75 hPa for high pressure (low altitude) clouds that dominate the population. There is also a branch of OMI RRS retrievals with higher OCPs than those from the $R^3S$ CloudSat simulation. We will examine these points in more detail below.

## 4 Fast cloud optical centroid pressure (OCP) simulator

### 4.1 Cloud OCP formulations

The cloud OCP, within the context of the Lambertian-Equivalent Reflectivity (LER) model, is defined as the pressure at which a Lambertian surface is placed in order to provide the observed amount of absorption (e.g., from oxygen) or filling-in due to rotational-Raman scattering. The Mixed LER (MLER) model further specifies a weighting of clear and cloudy subpixels with the effective cloud fraction as given by Eq. 1. The resulting cloud OCP, $P_{OCP}$, can be used to approximate the mean photon path-length of a more complex scenario in which there could be partial or thin clouds and the clouds may be geometrically thick and inhomogeneous (e.g., Koelemeijer et al., 2001; Vasilkov et al., 2008; Stammes et al., 2008; Ziemke et al., 2009).

The mean or centroid "optical pressure" of a complex cloud can be estimated by considering the relative contributions to e.g., rotational-Raman scattering or $O_2$ absorption from all scattering layers. Consider a simple scenario for a cloud optical centroid pressure retrieval making use of a pressure- and temperature-independent absorber with a constant mixing ratio in an atmosphere with no Rayleigh scattering. In a well-mixed layer, the column amount of the absorbing gas is proportional to the layer pressure thickness $\Delta P$. Absorption in the atmospheric layer is proportional to the col-

umn amount of the absorber. It follows that satellite-observed radiance backscattered from a cloud layer $L$ at a mean pressure $P_L$ undergoes an amount of absorption that is proportional to $\Delta P_L$, where $\Delta P_L$ is the layer thickness from the top of the atmosphere ($P_0 = 0$) to pressure $P_L$ ($\Delta P_L$=$P_L$).

For a given cloud or aerosol optical extinction profile, one may compute cloud/aerosol layer reflectances and transmittances, $r_L$ and $t_L$, respectively, from a layer $L$ using, for example, a two-stream model. While such a simple model cannot be used for computing accurate absolute quantities, it appears to be appropriate for providing relative values. It is the relative values that are most important for estimating the cloud OCP. Here, we use the delta-Eddington approximation of Joseph et al. (1976) with diffuse illumination. We then compute a reflectance contribution, $\rho_L$, from layer $L$ to the total cumulative reflectance using

$$\rho_L = \frac{r_L T_{L-1}^2}{(1 - R_{L-1} r_L)}, \tag{2}$$

where $R_L$ and $T_L$ are cumulative reflectances and transmittances, respectively, from the top-of-atmosphere to layer $L$, given by

$$R_L = \sum_{l=1}^{L} \rho_l \tag{3}$$

and

$$T_L = \frac{T_{L-1} t_L}{1 - R_{L-1} r_L}, \tag{4}$$

and $T_0 = 1$, $R_0 = 0$.

The cloud OCP ($P_{OCP}$) may then be approximated as a weighted-average over all layers $L$ from the top-of-atmosphere to the surface, where the weighting factor is given by $\rho_L$, i.e.,

$$P_{OCP} \simeq \frac{\sum_l \rho_l P_l}{\sum_l \rho_l}. \tag{5}$$

This formulation would produce an observed amount of absorption weighted by the same factor, i.e., an amount of absorption equivalent to that obtained when a single geometrically-thin, optically-thick cloud layer is placed at a pressure of $P_{OCP}$.

We tested several other methods for computing layer reflectances and transmittances. All methods provided very similar OCP values; although absolute reflectances and transmittances may be somewhat different for the different methods, the relative values as a function of layer, were not significantly different. We also compared OCPs computed with single scattering albedos of 1.0 and 0.99. Again, the relative values of layer reflectances/transmittances did not change enough to make significant differences in computed cloud OCPs.

The fast simulator may also be modified to account for properties of different cloud OCP retrievals. For example, the weighting scheme may modified as follows to simulate a cloud OCP from a retrieval based on an absorber with a pressure-squared dependence ($P'_{OCP}$) such as the oxygen dimer, e.g.,

$$P'_{\mathrm{OCP}} \simeq \sqrt{\frac{\sum_l \rho_l P_l^2}{\sum_l \rho_l}}. \tag{6}$$

We compared OCPs computed with the standard (Eq. 5) and pressure-squared (Eq. 6 formulations using profiles from one day of CloudSat data. We found that the pressure-squared formulation gave OCPs on average about 7 hPa higher (lower altitude) than the standard formulation with a standard deviation of 11 hPa and a maximum difference of 101 hPa.

### 4.2 Comparison of fast and full cloud OCP simulators

Figure 2 compares fast simulator results with those from the full rotational-Raman retrieval simulator ($R^3S$) for the same sample as CloudSat profiles used above in figure 1. The $R^3S$ incorporates errors in the rotational-Raman cloud algorithm resulting from the use of the MLER model. Such errors have been previously reported in Vasilkov et al.

(2008). These errors are largest for low cloud optical thicknesses. $R^3S$ results also account for the effects of enhanced photon pathlengths due to Rayleigh scattering within clouds and between cloud layers that are not accounted for with the fast simulator as shown in Fig. 5. Considering the simplicity of the fast simulator and the errors present in $R^3S$, the agreement between the two is quite good, with bias 7.4 hPa, standard deviation of 82 hPa, and correlation coefficient of 0.89.

### 4.3 Single day comparison of Cloudsat-based fast simulator with OMI RRS retrievals

Figure 3 shows a comparison of OMI cloud RRS retrievals with the fast OCP simulator for the same sample used in comparisons with $R^3S$ in Fig. 1. Here, we see a slightly larger bias for high pressure (low altitude) clouds as compared with $R^3S$. This is the result of a high bias in the fast simulator with respect to the full $R^3S$ simulator as shown in Fig. 2. $R^3S$ should better simulate actual OMI cloud RRS retrievals including errors due to the use of the MLER model. We also see larger biases in the opposite direction for the lower pressure clouds. Again, this is consistent with expected bias in the fast simulator. Although the full $R^3S$ provides a somewhat better agreement with OMI RRS retrievals than the fast simulator, the latter provides reasonable estimates of cloud OCP at a fraction of the computational cost; the full $R^3S$ takes more than one day for these calculations on a single state-of-the-art processor, wherease the fast simulator takes a few seconds.

### 4.4 Cloud OCP weighting functions

In Eq. 5, $\rho$ can be physically interpreted as a pressure weighting function. In other words, it weights a layer $L$ with mean pressure $P_L$ by the reflectance contribution from that layer, $\rho_L$. Next, we examine weighting functions calculated for one of the cloud scenarios used by Sneep et al. (2008) to investigate the behavior of four different cloud OCP algorithms; both the OMI RRS and O2-O2 algorithms were included as well as

two oxygen A band algorithms. In this example, the cloud is located between 550 and 800 hPa. As in Sneep et al. (2008), we use two different total cloud optical thicknesses, $\tau = 9$ and 42, where the optical thickness is equally distributed within the cloud. Sneep et al. (2008) showed that all algorithms produced OCPs near the geometric center of the cloud. For solar zenith angles (SZAs) of 30 and 40° and at a view zenith angle (VZA) of 30°, cloud OCPs were slightly higher for $\tau = 9$ as compared with $\tau = 42$. For higher SZAs and VZAs, differences between the $\tau = 9$ and $42$ were smaller.

Figure 4 shows examples of weighting functions produced for the above scenarios along with the cloud OCPs produced by the standard fast simulator. For both cloud optical thicknesses, the fast simulator places the cloud OCP in the middle of the cloud similar to the full simulations shown in Sneep et al. (2008). The fast simulator shows more photon penetration for the $\tau = 9$ case. For the $\tau = 42$ case, the fast simulator cloud OCP is weighted more towards to top part of the cloud.

Figure 5 shows sample weighting function and cloud OCP calculations for two different multi-layer extinction profiles from the CloudSat 2B-TAU product. These profiles are from a deep convective complex located in the tropical Pacific on 13 November 2006. The first profile shows a case where the upper layer has a large optical thickness ($\sim 50$). The cloud OCP weighting function peaks at a higher altitude than the cloud extinction profile. The standard fast cloud OCP simulation is close to the peak in the weighting function in the upper cloud deck; there is not much sensitivity of the cloud OCP to the lower cloud deck. The standard and pressure-squared weightings provide similar results in this case. The full $R^3S$ cloud OCP simulation is almost 150 hPa higher than the estimates from the fast simulators. This difference presumably results from enhanced photon pathlengths due to Rayleigh scattering within the cloud that is not accounted for in the fast simulators.

The lower panel shows an example where the standard and pressure-squared weightings provide slightly different results. This is another multi-layer cloud case, but here the top layer has a lower optical thickness ($\sim 6$). As a result, the weighting function shows significant sensitivity to the lower cloud deck. As expected, the pressure-squared

weighting provides more sensitivity to the lower cloud deck (higher pressure) than the standard weighting. Both fast cloud OCP simulations provide a value in the middle of the two cloud decks, with the pressure-squared weighting about 75 hPa higher. Here again, the full $R^3S$ provides a higher value of cloud OCP than both fast simulations.

## 5 Monthly Comparisons of CloudSat-based fast simulator OCPs with OMI retrievals

The fast simulator makes it more computationally feasible to do a large number of comparisons with CloudSat under a wide range of conditions. Such comparisons may reveal specific problems with the cloud OCP retrievals. However, in all comparisons of this type, we must bear in mind the expected differences between the fast simulator and the retrievals as shown for the RRS retrievals in Fig. 2.

Next, we compare CloudSat-based fast simulator cloud OCPs with retrievals from both OMI cloud algorithms for two months (January and July 2007). OMI RRS retrievals will be compared with results from the standard simulator and those from O2-O2 will be compared with results from the pressure-squared formulation. In this set of comparisons, we use a somewhat different scheme for averaging CloudSat data along the track for the length of the OMI pixel. Here, we compute a cloud OCP using our fast simulators (standard and pressure-squared versions) for each cloudy CloudSat sounding with total $\tau > 0.1$ that falls within an OMI pixel. We then compute a reflectance-weighted average OCP over the corresponding CloudSat pixels. In addition to the above-mentioned elimination of pixels for which the collocated MODIS cloud-top pressure standard deviation $>$ 100 hPa, we also eliminated pixels for which the along-track CloudSat-simulated OCP had a standard deviation $>$ 100 hPa. Since these pixels contain a large variability in cloud OCP along the CloudSat slice through the OMI pixel, the CloudSat slice may not be representative of the larger heteorogeneous OMI pixel.

### 5.1 Comparisons with CloudSat-based fast simulator over land

Figures 6-7 show comparisons between fast simulator CloudSat-based OCPs and the OMI RRS and O2-O2 cloud retrievals, respectively, over land for different bins of effective cloud fraction for July 2007. The effective cloud fraction is from the OMI RRS product and is used for all subsequent figures in order to provide the same sample for comparisons and computed statistics. Here again, we display the data in 2D histograms. Statistics for these and other comparisons are provided in Table 1.

There is reasonable agreement between CloudSat-simulated OCPs and those from both OMI algorithms. Slight biases between CloudSat and OMI RRS OCPs resemble those shown earlier that are produced from the fast simulator. However, as was also shown in Fig. 1, there is a cluster of pixels with CloudSat-based OCPs near 400 hPa for which both OMI algorithms retrieve significantly higher pressures. The differences are larger than those expected from the fast simulator.

The reduced scatter at higher effective cloud fractions can be explained as follows: Both random and systematic errors in the cloud OCP retrievals get amplified by a factor that is inversely proportional to the cloud radiance fraction ($f_r$), defined as the fraction of observed radiance that is due to cloud particles. Therefore, errors in cloud OCP approach infinity as $f_r$ goes to zero. The cloud radiance fraction can be estimated within the MLER context (see Eq. 1) using

$$f_r = f_{\text{eff}} \frac{I_{\text{cld}}}{I_{\text{obs}}}. \tag{7}$$

While $I_{cld}$ is relatively constant with wavelength (at the wavelengths considered here), $I_{obs}$ is wavelength dependent owing to variations in Rayleigh scattering and surface albedo. The much brighter Rayleigh scattering background in the UV (as compared with the visible) results in lower values of $f_r$ for the OMI RRS retrievals as compared with those from the O2-O2 for a given value of $f_{eff}$. Therefore, we expect greater error amplification for the RRS retrievals. Indeed, we observe slightly higher correlations between CloudSat and OMI O2-O2 than for Cloudsat versus OMI RRS. At the wave-

lengths used for the OMI RRS retrieval, $f_r \simeq 0.2 f_{eff}$ for $f_{eff} <\sim 0.3$. Therefore Errors at $f_{eff} = 5\%$ are about an order of magnitude higher than those at 100on data with moderate to high values of cloud radiance fraction.

We next examine the outliers, for which both OMI algorithms are biased high with respect to CloudSat, in more detail. These outliers appear in January (not shown here) as well as the single day in November 2006 that we examined in Fig. 1. A number of these cases appear to be caused by snow-covered pixels that are not correctly identified in the Near Real-time SSM/I EASE-Grid Daily Global Ice Concentration and Snow Extent (NISE) data set (Nolin et al., 1998) used in the OMI algorithms for snow/ice identification. Some of these cases coincide with storm clouds that may have produced fresh snow that has not yet been identified in the NISE data set.

Not all discrepancies between CloudSat and OMI cloud OCPs occurred near regions of snow-ice. An examination of the CloudSat profiles showed that many of these pixels contained multi-layered clouds. As shown in Fig. 5, these are the profiles for which the fast simulator has the largest difference with the full RRS simulator. The differences, however, are generally too large to be explained by the fast simulator alone. In many cases, multiple outliers occur within a close proximity where there is significant variability in the CloudSat-simulated cloud OCP as well as cloud-top pressure. In most cases, excess scattering and absorption produces higher than expected cloud OCPs in both OMI algorithms, indicating a geophysical effect rather than measurement or algorithm errors. We hypothesize that 3D cloud effects may be contributing to some of these differences.

### 5.2 Comparisons with CloudSat-based fast simulator over ocean

Figures 8-9 show comparisons similar to those in Figs. 6-7 but over ocean. Here, we see a predominance of low altitude (high pressure) clouds for moderate values of cloud effective fraction. A bimodal distribution in the low clouds with peaks near 775 and 875 hPa is apparent for effective cloud fractions between 25 and 50%. This bimodality, a prevalent feature of trade wind cumulus clouds, has been observed in several different

passive satellite cloud-top height data sets, both thermal IR and stereo algorithms, as well as surface ceilometer cloud base height measurements (e.g., Genkova et al., 2007; Mote and Frey, 2006). High altitude (low pressure) clouds are prevalent only for high effective cloud fractions. As over land, though not as distinct, for both OMI algorithms we see a cluster of points with higher a cloud OCP than predicted from CloudSat/MODIS.

### 5.3 Comparisons of two OMI cloud algorithms over land and ocean

Figures 10 and 11 show similar 2D histograms for the same sample of pixels as above, but now for the OMI RRS versus O2-O2 cloud OCPs for land and ocean, respectively. The O2-O2 OCPs are slightly higher than those from RRS retrievals. There are skews in the distributions particularly over ocean where the O2-O2 algorithm provides higher cloud OCPs than those from the RRS algorithm.

The scatter between the two OMI cloud OCPs is significantly smaller than either one compared with CloudSat. The OMI algorithms are nearly independent; they operate on on different physical principles and use two separate detectors. Therefore, our results strongly indicate that consistent differences between CloudSat and both OMI cloud OCPs are not due to algorithm or measurement error but rather to geophysical effects, such as cloud 3D effects including the cloud adjacency effect discussed by Marshak et al. (2008).

### 5.4 Probability Distribution Functions (PDFs) of cloud OCP

Figure 12 shows the above results for July 2007 displayed as probability distribution functions (PDFs) of cloud OCPs computed from CloudSat 2B-TAU data using the fast simulator and those from both OMI cloud algorithms for both land and ocean and derived using only pixels with effective cloud fractions $> 0.3$. The OMI distributions are similar to those shown previously by Sneep et al. (2008). Over ocean, CloudSat shows a trimodal distribution with a small peak 400 hPa. Both OMI algorithms only hint at a

low pressure mode, with a higher pressure than that given by CloudSat. As noted earlier for high pressure clouds, there are peaks in the distribution near 775 and 875 hPa in the CloudSat-derived OCPs. The OMI RRS algorithm underestimates the pressure of these clouds while the OMI O2-O2 algorithm overestimates. Neither OMI cloud algorithm shows a clear bimodal distribution in the high pressure clouds, though there is a hint of bimodality in the OMI RRS PDF. Genkova et al. (2007) showed that distributions of cloud top heights of trade wind cumulus derived from thermal IR measurements are affected by spatial resolution. It should be noted that the OMI pixel is twice as wide in the cross-track direction as the length along track over which the CloudSat OCPs are averaged.

Over land, the CloudSat OCP PDF is bimodal with peaks near 400 and 600 hPa. Similar bimodal distributions of cloud top pressure and vertical structure have been shown with both active and passive sounding data as well as in general circulation model output (e.g., Chang and Li, 2005a,b; Comstock and Jakob, 2004; Mote and Frey, 2006; Xi et al., 2010). Neither OMI algorithm produces a bimodal distribution; both produce a single peak between 650 and 700 hPa. The RRS PDF is more sharply peaked, while the O2-O2 produces more high pressure clouds.

### 5.5 Maps of cloud OCP and effective cloud fraction

Figure 13 show gridded maps of effective cloud fraction from the OMI RRS algorithm and cloud OCP from CloudSat for the pixels collocated with CloudSat in July 2007. This provides a context for maps of the differences between CloudSat-based OCPs and those from OMI RRS and O2-O2, respectively, shown in Figures 14 and 15. These figures also show corresponding histograms. The difference maps show all individual points (i.e., not gridded data). Each point is color coded by the corresponding histogram bin, where the color scale is chosen to emphasize positive versus negative biases.

In the histograms, the skew of the distribution is seen here for both OMI algorithms versus CloudSat for land as well as ocean, as shown in previous figures. The maps

provide the geographic distribution of the differences. It is now apparent that most of the positive differences with respect to the RRS cloud OCPs over ocean occur in regions where subsidence produces low clouds and relatively low cloud effective fractions. The high cloud OCPs seen in the inter-tropical convergence zone (ITCZ) show negative differences. Similar patterns are seen with respect to the OMI O2-O2 retrievals. However, more pronounced negative differences are seen at high southern latitudes. Both OMI algorithm produce negative differences with respect to CloudSat at high northern latitudes.

Figures 16-18 show a similar series for January 2007. The spatial patterns of differences with CloudSat are similar to July in the tropics. At moderate to high latitudes, the patterns have reversed with respect to the hemispheres; both algorithm produce negative differences with respect to CloudSat at high southern latitudes, while O2-O2 has more prominent negative differences at high northern latitudes.

## 6 Conclusions

We have developed a relatively simple scheme for simulating retrieved cloud optical centroid pressures from satellite solar backscatter observations. We have compared simulator results with those from more detailed retrieval simulators that more fully account for the complex radiative transfer in a cloudy atmosphere.

We used this fast simulator to conduct a comprehensive evaluation of cloud OCPs from the two OMI algorithms using collocated data from CloudSat and Aqua MODIS, a unique situation afforded by the A-train formation of satellites. We find that both OMI algorithms perform reasonably well and that the two algorithms agree better with each other than either does with the collocated CloudSat data. This indicates that patchy snow/ice, cloud 3D, and aerosol effects not simulated with the CloudSat data are affecting both algorithms similarly. We note that the collocation with CloudSat occurs mainly on the East side of OMI's swath. Therefore, we are not able to address cross-track biases in OMI cloud OCP retrievals.

Our fast simulator may also be used to simulate cloud OCP from output generated by general circulation models (GCM) with appropriate account of cloud overlap. We have implemented such a scheme and plan to compare OMI data with GCM output in the near future.

*Acknowledgements.* This material is based upon work supported by the National Aeronautics and Space Administration under agreement NNG06HX18C issued through the Science Mission Directorate for the Aura Science Team. We thank the OMI, MODIS, and CloudSat data processing teams for providing the data used for this study.

## References

Acarreta, J. R., de Haan, J. F. and Stammes, P.: Cloud pressure retrieval using the $O_2$-$O_2$ absorption band at 477 nm, J. Geophys. Res., 109, D05204, doi: 10.1029/2003JD003915, 2004.

Ahmad, Z., Bhartia, P. K., and Krotkov, N.: Spectral properties of backscattered UV radiation in cloudy atmospheres, J. Geophys. Res., 109, D01201, doi:10.1029/2003JD003395, 2004.

Baum, B. A., Yang, P., Heymsfield, A. J., Platnick, S., King, M. D., Hu, Y. X., and Bedka, S. T.: Bulk scattering models for the remote sensing of ice clouds. Part 2: Narrowband models, J. Appl. Meteorol., 44, 1896–1911, 2005.

Bovensmann, H., Burrows, J., Buchwitz, M., Frerick, J., Noel, S., Rozanov, V., Chance, K., and Goede, A.: SCIAMACHY: mission objectives and measurement modes, J. Atmos. Sci., 56, 127–150, 1999.

Bucsela, E. J., Celarier, E. A., Wenig, M. O., Gleason, J. F., Veefkind, J. P., Boersma, K. F., and Brinksma, E. J.: Algorithm for $NO_2$ vertical column retrieval from the Ozone Monitoring Instrument, IEEE Trans. Geosci. Remote Sens., 44, 1245–1258, 2006.

Burrows, J. P., Weber, M., Buchwitz, M., Rozanov, V., Ladstatter-Weissenmayer, A., Richter, A., deBeek, R., Hoogen, R., Bramstedt, K., Eichmann, K.-U., Eisinger, M., and Perner, D.: The Global Ozone Monitoring Experiment (GOME): Mission concept and first scientific results, J. Atmos. Sci., 56, 151–175, 1999.

Chang F.-L. and Li, Z.: A new method for detection of cirrus overlapping water clouds and determination of their optical properties, J. Atmos. Sci., 62, 3993–4009, 2005.

Chang F.-L. and Li, Z.: A near-global climatology of single-layer and overlapped clouds and their optical properties retrieved from Terra/MODIS data using a new algorithm, J. Climate, 18, 4572–4771, 2005.

Coldewey-Egbers, M., Weber, M., Lamsal, L. N., de Beek, R., Buchwitz, M., and Burrows, J. P.: Total ozone retrieval from GOME UV spectral data using weighting function DOAS approach, Atmos. Chem. Phys., 5, 1015–1025, 2005.

CloudSat Project: Level 2 cloud optical depth product process description and interface control document, version 5.0, http://www.cloudsat.cira.colostate.edu/ICD/2B-TAU/2B-TAU_PDICD_5.0.pdf, Colorado State Univeristy, CO, USA, 2008.

Comstock, J. M., Jakob, C.: Evaluation of tropical cirrus cloud properties derived from ECMWF model output and ground based measurements over Nauru Island, Geophys. Res. Lett., 31, L10106, doi:10.1029/2004GL019539, 2004.

Cox, C., and Munk, W.: Measurement of the roughness of the sea surface from photographs of the Sun's glitter, J. Opt. Soc. Amer., 44, 838–850, 1954.

Daniel, J. S., Solomon, S., Miller, H. L., Langford, A. O., Portmann, R. W., and Eubank, C. S.: Retrieving cloud information from passive measurements of solar radiation absorbed by molecular oxygen and $O_2$–$O_2$, J. Geophys. Res., 108, 4515, doi:4510.1029/2002JD002994, 2003.

Deirmendjian, D.: Electromagnetic scattering on spherical polydispersions, Elsevir Sci., New York, 290 pp., 1969.

Dubuisson, P., Frouin, R., Dessailly, D., Duforêt, L,: Altitude of aerosol plumes over the ocean from reflectance ratio measurements in the $O_2$ A-band, Remote Sens. Environ., 113, 1899–1911, 2009.

Genkova, I., Seiz, G., Zuidema, P., Zhao, G., Di Girolamo, L.: Cloud top height comparisons from ASTER, MISR, and MODIS for trade wind cumuli, Remote Sens. Environ., 107, 211-222, 2007.

Joiner J., and Bhartia, P. K.: Accurate Determination of Total Ozone using SBUV Continuous Spectral Scan Measurements, J. Geophys. Res., 102, 12,957-12,969, 1995.

Joiner, J., Vasilkov, A. P., Flittner, D. E., Gleason, J. F., and Bhartia, P. K.: Retrieval of cloud chlorophyll content using Raman scattering in GOME spectra, J. Geophys. Res., 109, D01109, doi:10.1029/2003JD003698, 2004.

Joiner, J. and Vasilkov, A. P.: First results from the OMI rotational raman scattering cloud pressure algorithm, IEEE T. Geosci. Remote, 44, 1272–1282, 2006.

Joiner, J., Vasilkov, A. P., Yang, K. and Bhartia, P. K.: Total column ozone over hurricanes from the ozone monitoring instrument, Geophys. Res. Lett., 33, L06807, doi:10.1029/2005GL0255922006, 2006.

Joiner, J., Schoeberl, M. R., Vasilkov, A. P., Oreopoulos, L., Platnick, S., Livesey, N. J., and Levelt, P. F.: Accurate satellite-derived estimates of the tropospheric ozone impact on the global radiation budget, Atmos. Chem. Phys., 9, 4447–4465, 2009.

Joiner, J., Vasilkov, A. P., Bhartia, P. K., Wind, G., Platnick, S., and Menzel, W. P.: Detection of multi-layer and vertically-extended clouds using A-train sensors, Atmos. Meas. Tech., 3, 233–247, 2010.

Joseph, J. H., Wiscombe, W. J., Weinman, J. A.: The delta-Eddington approximation for radiative flux transfer, J. Atmos. Sci., 33, 2452–2459, 1976.

Koelemeijer, R. B. A. and Stammes, P.: Effects of clouds on ozone column retrieval from GOME UV measurements, J. Geophys. Res., 104, 8281–8294, 1999.

Koelemeijer, R. B. A., Stammes, P., Hovenier, J. W., and de Haan, J. F.: A fast method for retrieval of cloud parameters using oxygen A-band measurements from the Global Ozone Monitoring Experiment, J. Geophys. Res., 106, 3475-3496, 2001.

Koelemeijer, R. B. A., Stammes, P., Hovenier, J. W., and de Haan, J. F.: Global distribution of effective cloud fraction and cloud top pressure derived from oxygen A band measured by the Global Ozone Monitoring Experiment: Comparison to ISCCP data, J. Geophys. Res., 107, 4151, doi:10.1029/2001JD0000840, 2002.

Kokhanovsky, A. A., Rozanov V. V., Nauss, T., Reudenback, C., Daniel, J. S., Miller, H. L., and Burrows, J. P.: The semianalytical cloud retrieval algorithm for SCIAMACHY. 1. The validation, Atmos. Chem. Phys., 6, 1905–1911, 2006.

Kokhanovsky, A. A., Mayer, B., Rozanov, V. V., Wapler, K., Burrows, J. P., and Schumann, U.: The influence of broken cloudiness on cloud top height retrievals using the nadir observations of backscattered solar radiation in the oxygen A-band, J. Quant. Spectrosc. Rad. Trans., 103, 460–477, 2007.

Kokhanovsky, A. A., Mayer, B., Rozanov, V. V., Wapler, K., Lamsal, L. N., Weber, M., Burrows, J. P., and Schumann, U.: Satellite ozone retrieval under broken cloud conditions: An error analysis based on Monte Carlo simulations, IEEE Trans. Geosci. Remote, 45, 187–194, 2007.

Levelt, P. F., van der Oord, G. H. J., Dobber, M. R., Malkki, A., Visser, H., de Vries, J., Stammes, P., Lundell, J. O. V., and Saari, H.: The ozone monitoring instrument, IEEE T. Geosci. Re-

mote, 44, 1093–1101, 2006.
Marshak, A., Wen, G., Coakley, J. A., Remer, L. A., Loeb, N. G., and Cahalan, R. F.: A simple model for the cloud adjacency effect and the apparent bluing of aerosols near clouds, J. Geophys. Res., 113, D14S17, doi:10.1029/2007JD009196, 2008.
McPeters, R. D., Bhartia, P. K., Krueger, A. J., Herman, J. R., Schlesinger, B. M., Wellemeyer, C. G., Seftor, C. J., Jaross, G., Taylor, S. L., Swissler, T., Torres, O., Labow, G., Byerly, W., and Cebula, R. P.: Nimbus-7 Total Ozone Mapping Spectrometer (TOMS) data products user's guide, NASA Ref. Pub. 1384, Washington, DC, USA, 67 pp., 1996.
Menzel, W. P., Frey, R., Zhang, H., Wylie, D. P., Moeller, C., Holz, R., Maddux, B., Baum, B. A., Strabala, K. I., and Gumley, L.: MODIS global cloud-top pressure and amount estimation: algorithm description and results, J. Appl. Meteorol. Clim., 47, 1175–1198, 2008.
Mote, P. W., and Frey, R.: Variability of clouds and water vapor in low latitudes: View from Moderate Resolution Imaging Spectroradiometer (MODIS), J. Geophys. Res., 111, D16101, doi:10.1029/2005JD006791, 2006.
Munro, R., Eisinger, M., Anderson, C., Callies, J., Corpaccioli, E., Lang, R., Lefebvre, A., Livschitz, Y., and Perez Albinana, A.: GOME-2 on Metop: from in-orbit verification to routine operations, in: Proceedings of EUMETSAT Meteorological Satellite Conference, Helsinki, Finland, 12–16 June 2006.
Nolin, A., Armstrong, R. L., and Maslanik, J.: Near Real-Time SSM/I EASE-Grid Daily Global Ice Concentration and Snow Extent, Jan to Mar 2004 (updated daily), Boulder, CO, USA: National Snow and Ice Data Center, Digital media, 1998.
Reuter, M., Buchwitz, M., Schneising, O., Heymann, J., Bovensmann, H., and Burrows, J. P.: A method for improved SCIAMACHY $CO_2$ retrieval in the presence of optically thin clouds, Atmos. Meas. Tech., 3, 209–232, 2010.
Roozendael van, M., Loyola, D., Spurr, R., Balis, D., Lambert, J.-C., Livschitz, Y., Valks, P., Ruppert, T., Kenter, P., Fayt, C., and Zehner, C.: Ten years of GOME/ERS-2 total ozone data-The new GOME data processor (GDP) version 4: 1. Algorithm description, J. Geophys. Res., 111, D14311, doi:10.1029/2005JD006375, 2006.
Rozanov, V. V. and Kokhanovsky, A. A.: Semianalytical cloud retrieval algorithm as applied to the cloud top altitude and the cloud geometrical thickness determination from top-of-atmosphere reflectance measurements in the oxygen A band, J. Geophys. Res., 109, D05202, doi:10.1029/2003JD004104, 2004.
Rozanov, V. V., Kokhanovsky, A. A., and Burrows, J. P: The determination of cloud altitudes

using GOME reflectance spectra: multilayered cloud systems, IEEE T. Geosci. Remote, 42, 1009–1017, 2004.

Sneep, M., de Haan, J., Stammes, P., Wang, P., Vanbauce, C., Joiner, J., Vasilkov, A. P., and Levelt, P. F.: Three way comparison between OMI/Aura and POLDER/PARASOL cloud pressure products, J. Geophys. Res., 113, D15S23, doi:10.1029/2007JD008694, 2008.

Spurr, R. J. D., de Haan, J., van Oss, R., and Vasilkov, A. P.: Discrete ordinate radiative transfer in a stratified medium with first order rotational Raman scattering, J. Quant. Spectrosc. Ra., 109(3), 404–425, 2008.

Stammes, P., Sneep, M., de Haan, J. F., Veefkind, J. P., Wang, P., and Levelt, P. F.: Effective cloud fractions from the Ozone Monitoring Instrument: Theoretical framework and validation, J. Geophys. Res., 113, D16S38, doi:10.1029/2007JD008820, 2008.

Stephens, G. L., Vane, D. G., Taneli, S., et al.: CloudSat Mission: Performance and early science after the first year of operation, J. Geophys. Res., 113, D00A18, doi:10.1029/2008JD009982, 2008.

Vanbauce, C., Cadet, B., and Marchand, R. T.: Comparison of POLDER apparent and corrected oxygen pressure to ARM/MMCR cloud boundary pressures, Geophys. Res. Lett., 3, 1212, doi:10.1029/2002GL016449, 2003.

Vasilkov, A. P., Joiner, J., Yang, K., and Bhartia, P. K.: Improving total column ozone retrievals by using cloud pressures derived from Raman scattering in the UV, Geophys. Res. Lett., 31, L20109, doi:10.1029/2004GL020603, 2004.

Vasilkov, A. P., Joiner, J., Spurr, R., Bhartia, P. K., Levelt, P. F., and Stephens, G.: Evaluation of the OMI cloud pressures derived from rotational Raman scattering by comparisons with other satellite data and radiative transfer simulations, J. Geophys. Res., 113, D15S19, doi:10.1029/2007JD008689, 2008.

Vasilkov, A. P., Joiner, J., Oreopoulos, L., Gleason, J. F., Veefkind, P., Bucsela, E., Celarier, E. A., Spurr, R. J. D., and Platnick, S.: Impact of tropospheric nitrogen dioxide on the regional radiation budget, Atmos. Chem. Phys., 9, 6389–6400, 2009.

Veefkind, J. P., de Haan, J. F., Brinksma, E. J., Kroon, M., and Levelt, P.: Total ozone from the Ozone Monitoring Instrument (OMI) using the DOAS technique, IEEE T. Geosci. Remote Sens., 44, 1239–1244, 2006.

Ziemke, J. R., Joiner, J., Chandra, S., Bhartia, P. K., Vasilkov, A., Haffner, D. P., Yang, K., Schoeberl, M. R., Froidevaux, L., and Levelt, P. F.: Ozone mixing ratios inside tropical deep convective clouds from OMI satellite measurements, Atmos. Chem. Phys., 9, 573–583, 2009.

Xi, B., Dong, X., Minnis, P., and Khaiyer, M. M.: A 10 year climatology of cloud fraction and vertical distribution derived from both surface and GOES observations over the DOE ARM SPG site, J. Geophys. Res., 115, D12124, doi:1029/2009JD012800, 2010.

**Table 1.** Monthly-mean cloud OCP comparison statistics including average (mean) difference, standard deviation of the difference ($\sigma$), both in hPa, and correlation coefficient, R, for July 2007, where CS stands for OCPs from CloudSat profiles run through the fast simulator.

| | 0.50<ECF<0.75 | | | 0.75<ECF<1.0 | | |
|---|---|---|---|---|---|---|
| Data sets, conditions | avg. diff. | $\sigma$ | R | avg. diff. | $\sigma$ | R |
| Land | | | | | | |
| RRS–CS | 77 | 167 | .43 | 91 | 143 | .56 |
| $O_2O_2$–CS | 111 | 163 | .50 | 125 | 144 | .57 |
| RRS–$O_2O_2$ | -38 | 86 | .85 | -40 | 63 | .92 |
| Ocean | | | | | | |
| RRS–CS | 77 | 178 | .51 | 74 | 148 | .54 |
| $O_2O_2$–CS | 105 | 178 | .54 | 92 | 151 | .56 |
| RRS–$O_2O_2$ | -32 | 84 | .88 | -25 | 63 | .92 |

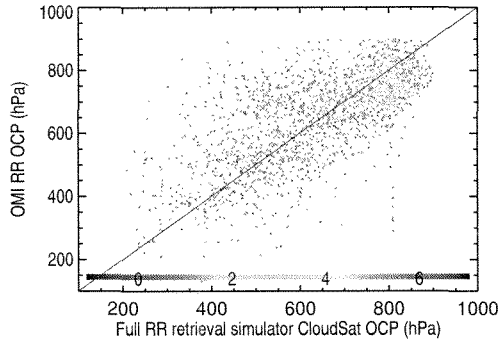


**Fig. 1.** Two dimensional histogram showing comparison between cloud OCPs from the actual OMI rotational-Raman scattering retrievals with those from the full rotational-Raman scattering simulator ($R^3S$) using CloudSat extinction profiles with $\tau > 5$ for a single day (13 November 2006). Results are provided as 2 dimensional densities in cloud pressure bins of 10 hPa. The color scale represents the number of pixels falling within a given bin.

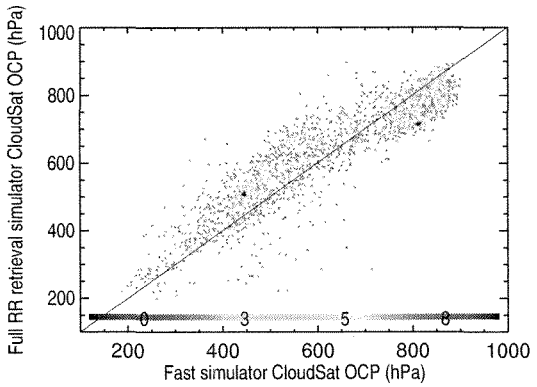


**Fig. 2.** Two dimensional histogram showing comparison between cloud OCPs from the fast simulator with those from the full rotational-Raman scattering simulator ($R^3S$) for the same sample of points used in Fig. 1.

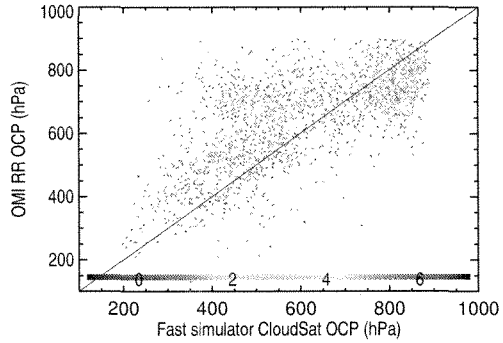


**Fig. 3.** Similar to Fig. 1 but comparing cloud OCPs from the OMI rotational-Raman retrievals with those from the fast simulator.

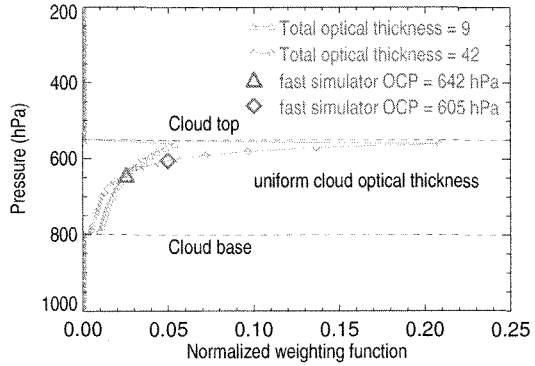


**Fig. 4.** Cloud OCPs and weighting functions for clouds with a uniform optical extinction profile and two different total optical thicknesses.

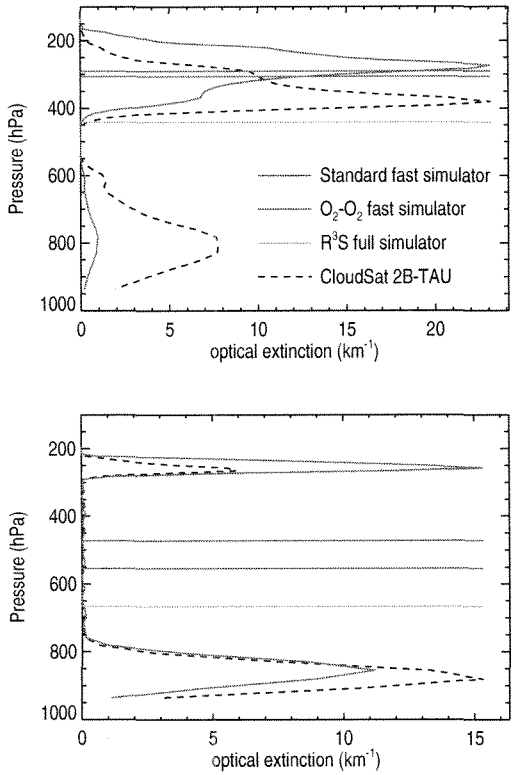


**Fig. 5.** Two examples of CloudSat cloud extinction profiles for multi-layer clouds: The top panel is for a case with an optically thick upper layer ($\tau \simeq 50$) while the bottom panel shows a case with an optically thin upper layer ($\tau \simeq 6$). Standard and $O_2$-$O_2$ fast simulator results are more similar for the optically thick upper layer; $O_2$-$O_2$ weights more heavily towards the lower layer when the upper layer is more optically thin.

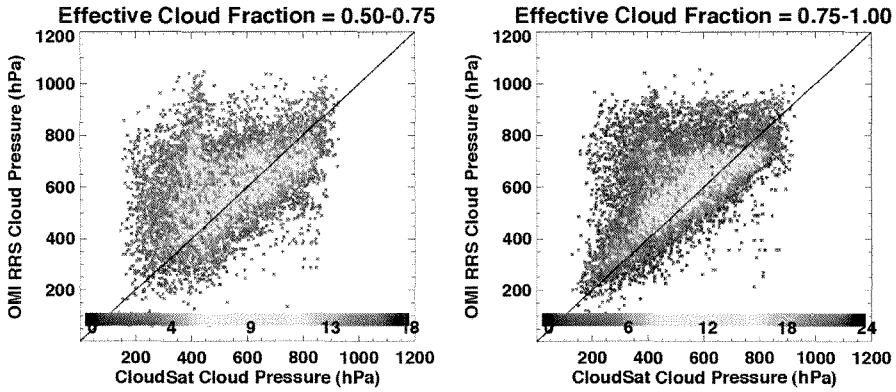


**Fig. 6.** Comparison of cloud pressures using a 2D histogram as in Fig. 2: CloudSat OCPs (based on 2B-TAU profiles and the fast simulator) with OMI RRS cloud OCP retrievals over land for different bins of effective cloud fraction for July 2007. Note that the color scale changes for the different cloud effective fraction bins.

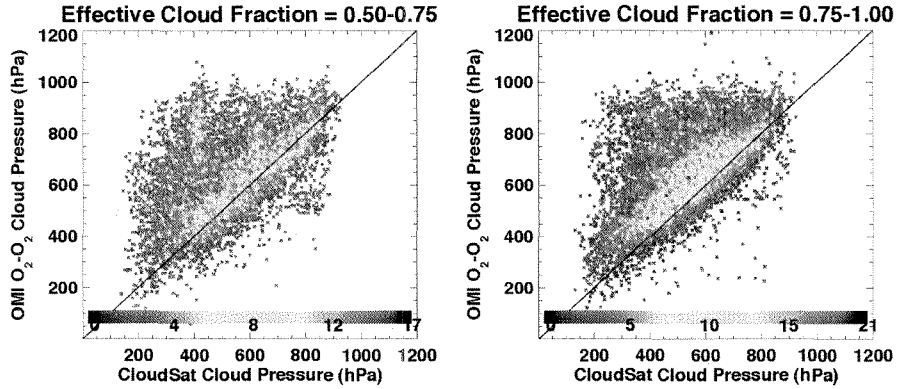


**Fig. 7.** Similar Fig. 6 but for OMI $O_2$-$O_2$ cloud OCP retrievals (over land).

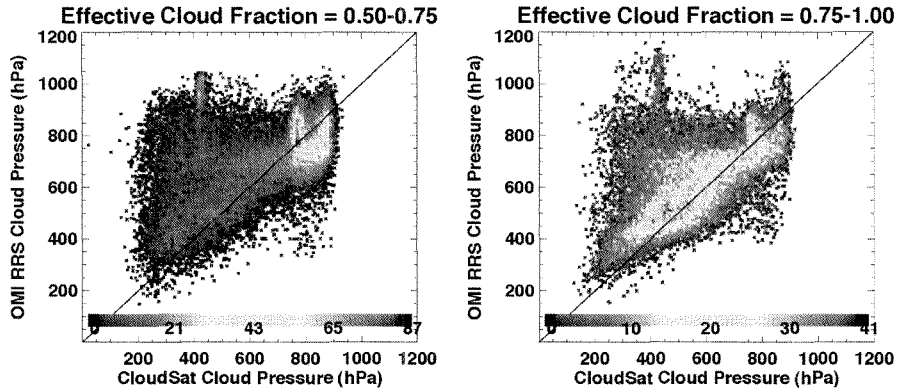


**Fig. 8.** Similar Fig. 6 but over ocean (July 2007)

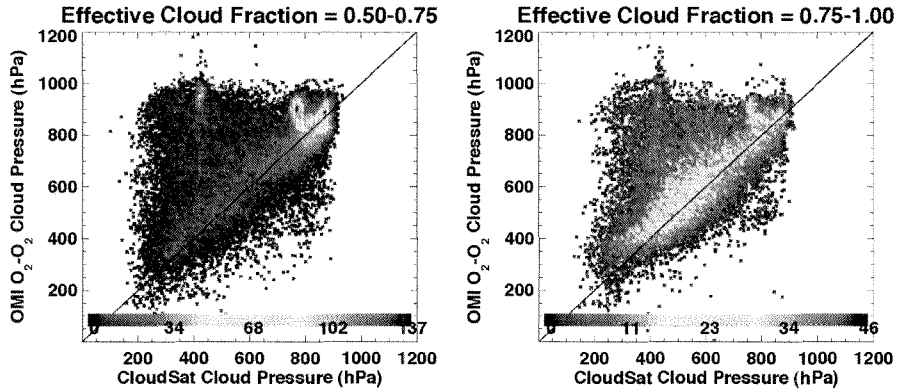


**Fig. 9.** Similar Fig. 8 but for $O_2$-$O_2$ (ocean, July 2007)

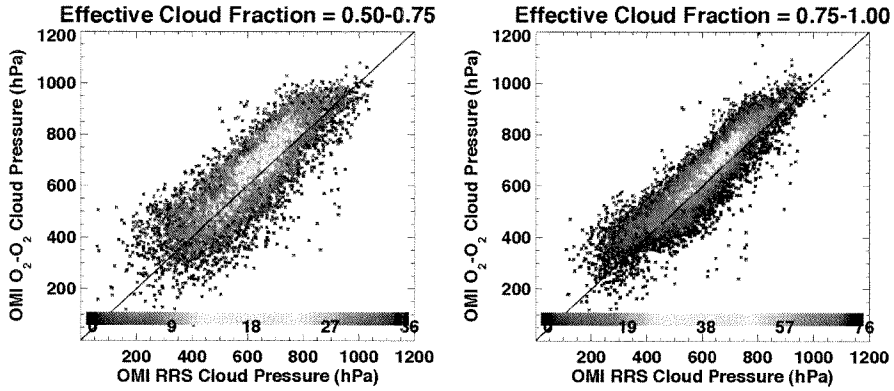


**Fig. 10.** Similar Fig. 6 (same sample of pixels) but comparing OMI cloud OCP retrievals from the RRS and $O_2$-$O_2$ products over land (July 2007).

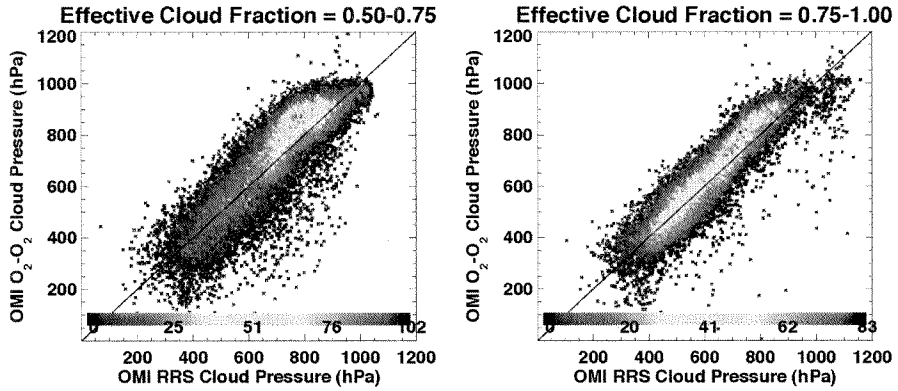


**Fig. 11.** Similar Fig. 10 (same sample of pixels) but over ocean (July 2007).

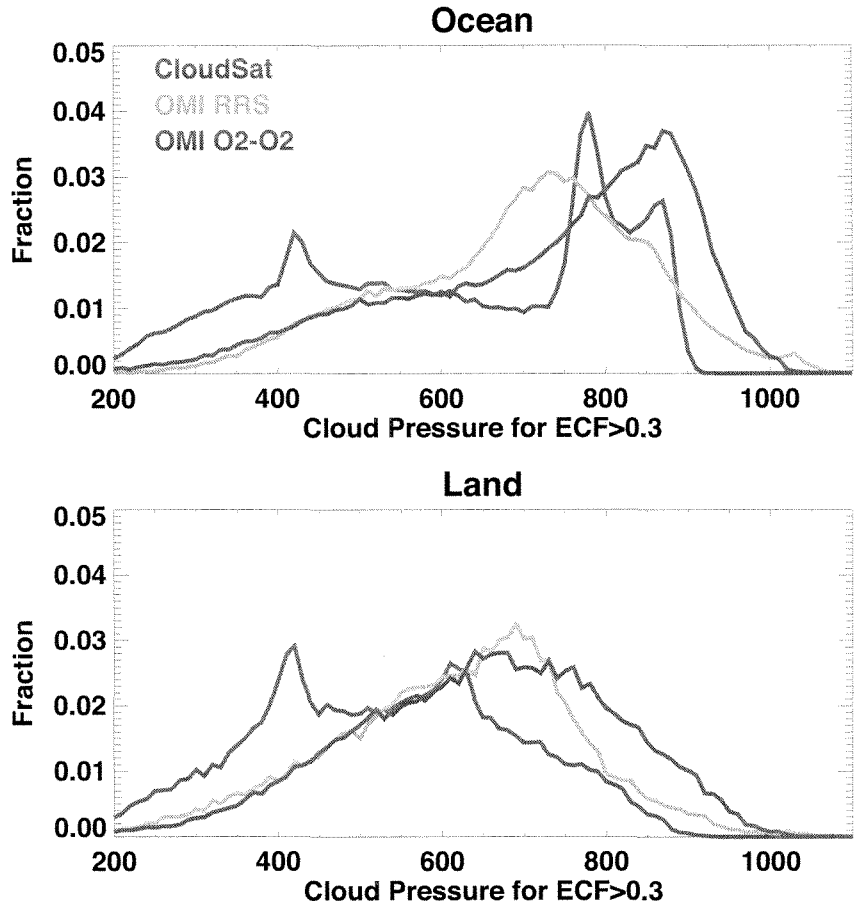


**Fig. 12.** Probability distribution functions of CloudSat cloud OCP (2B-TAU profiles with fast simulator) and the two OMI cloud algorithms over ocean (top) and land (bottom) for pixels with effective cloud fraction (ECF) $> 0.3$.

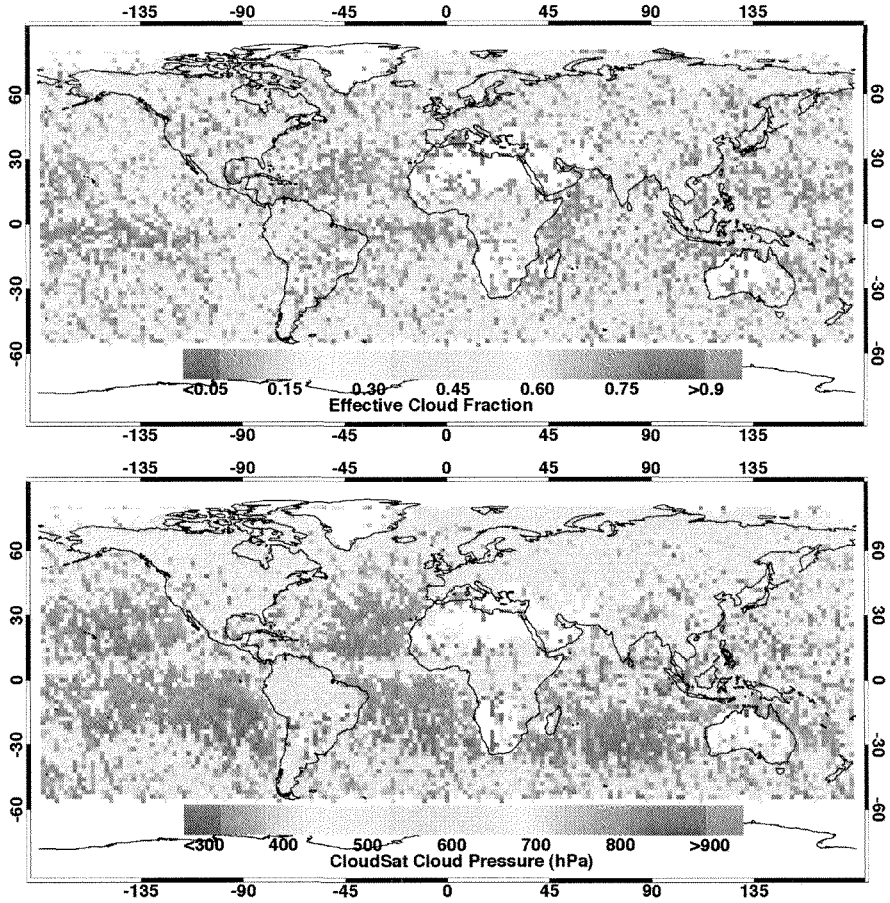


**Fig. 13.** Maps of gridded effective cloud fraction from the OMI cloud RRS algorithm (top) and cloud OCP from CloudSat (bottom) for July 2007.

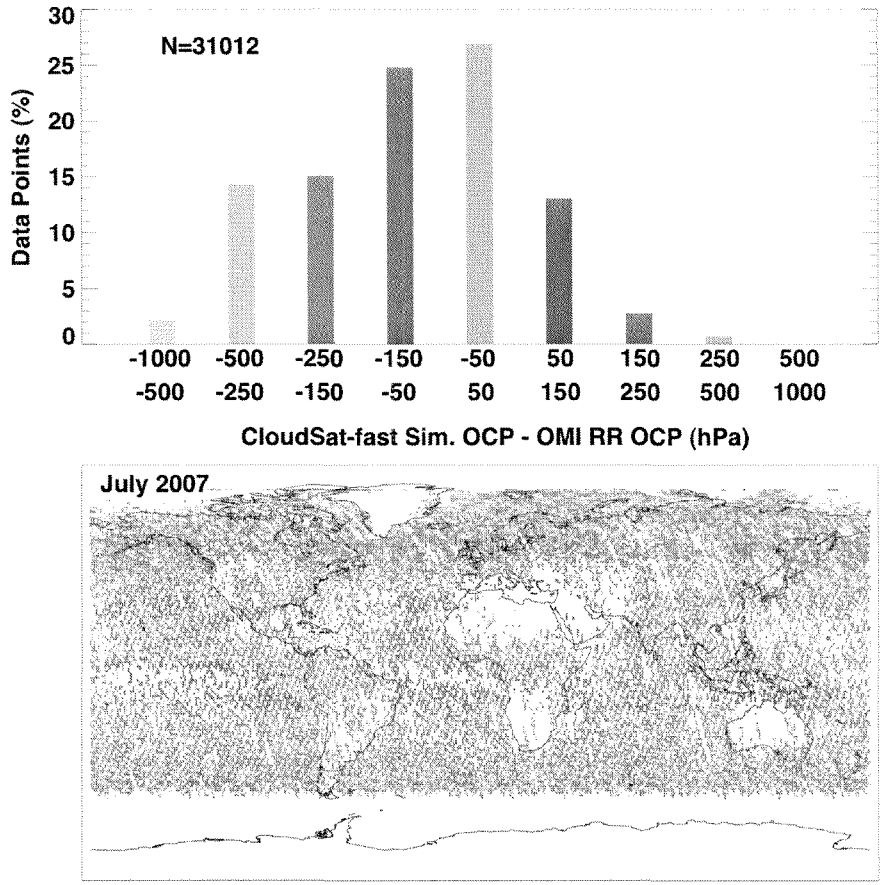


**Fig. 14.** Histogram (top) and color-coded map (bottom) of differences between CloudSat cloud OCP and that from the OMI RRS algorithm for effective cloud fractions $> 0.1$.

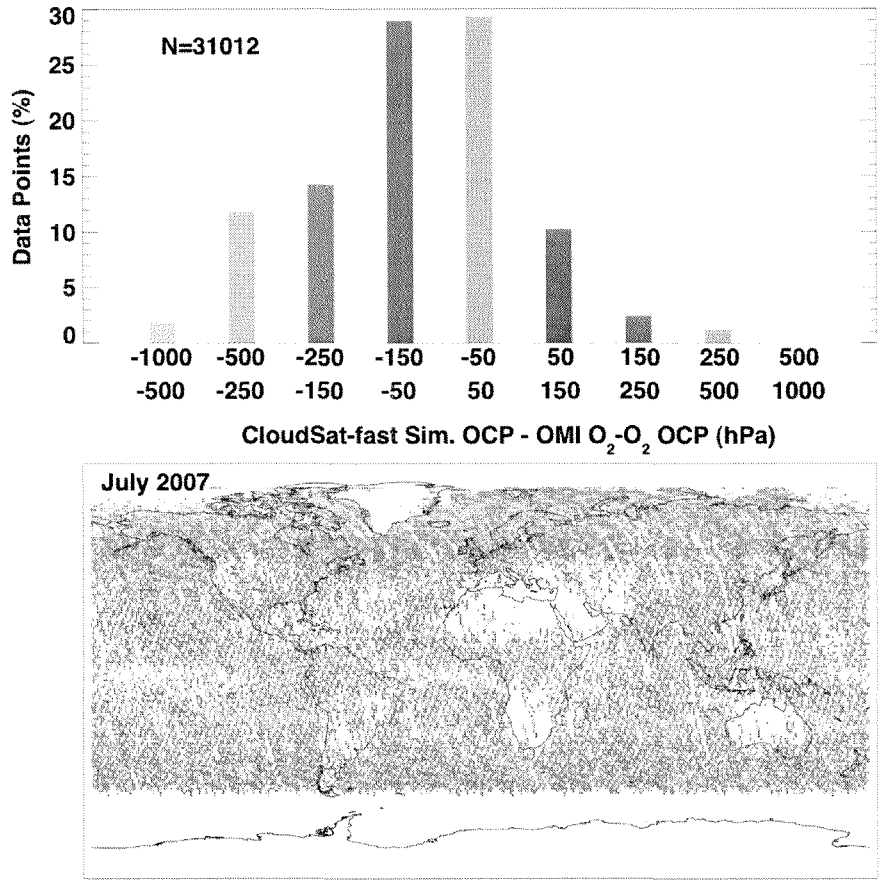


**Fig. 15.** Similar to Fig. 14, but for OMI $O_2$-$O_2$.

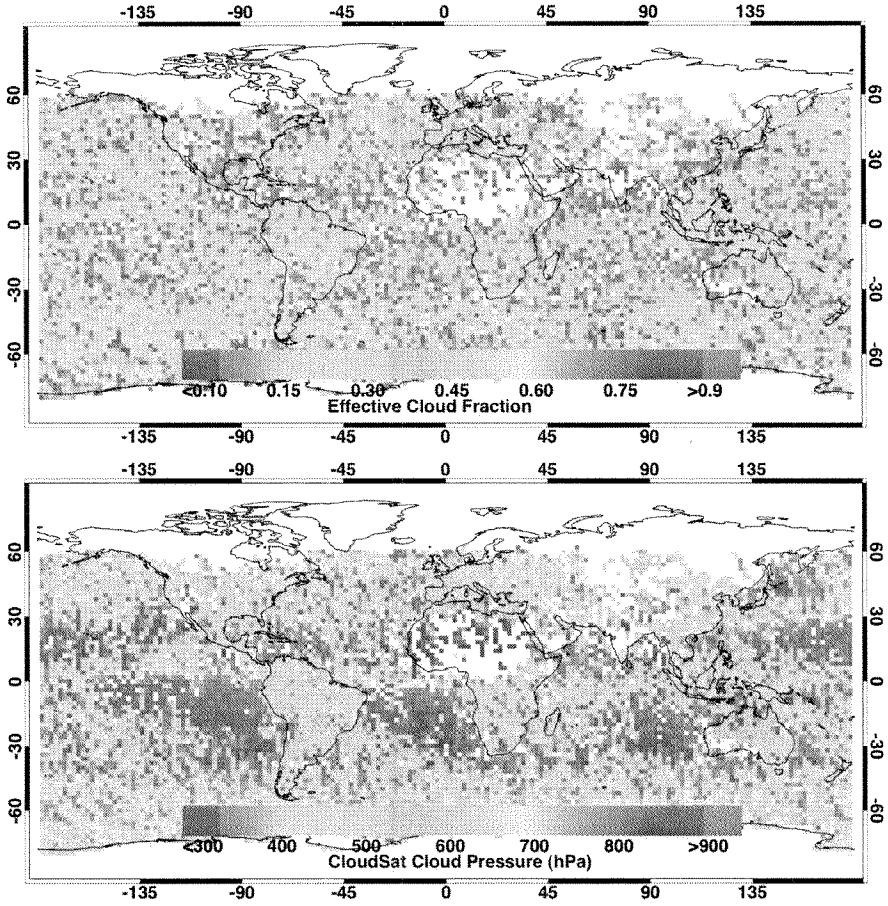


**Fig. 16.** Similar to Fig. 13 but for January 2007.

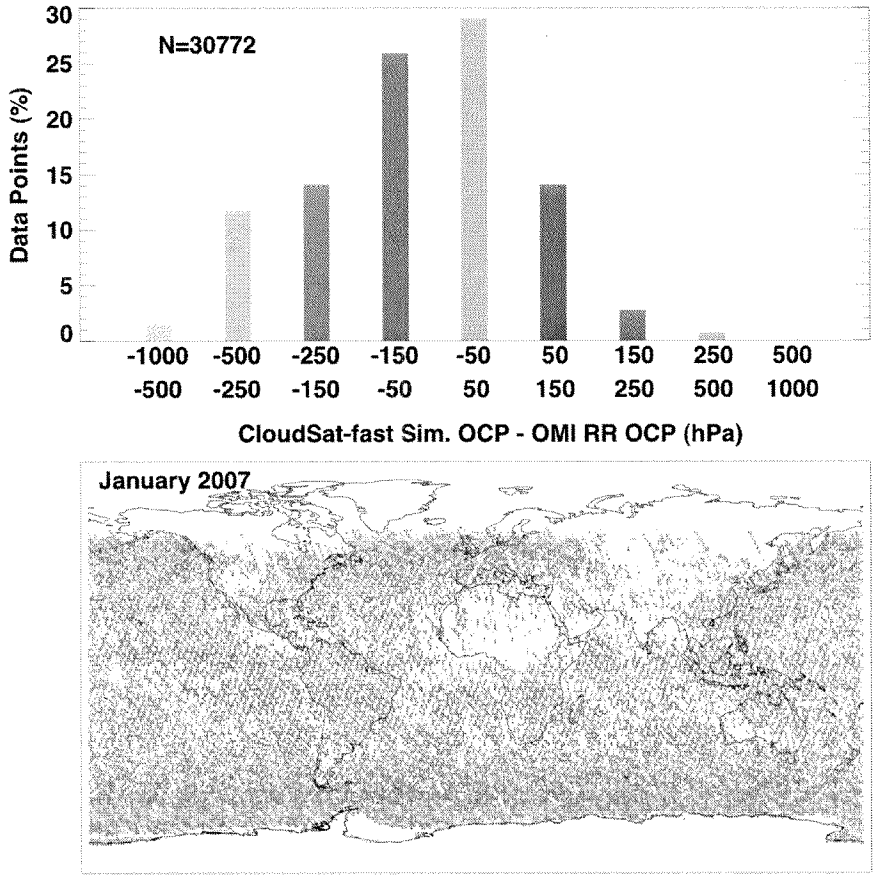


**Fig. 17.** Similar to Fig. 14, but for January 2007.

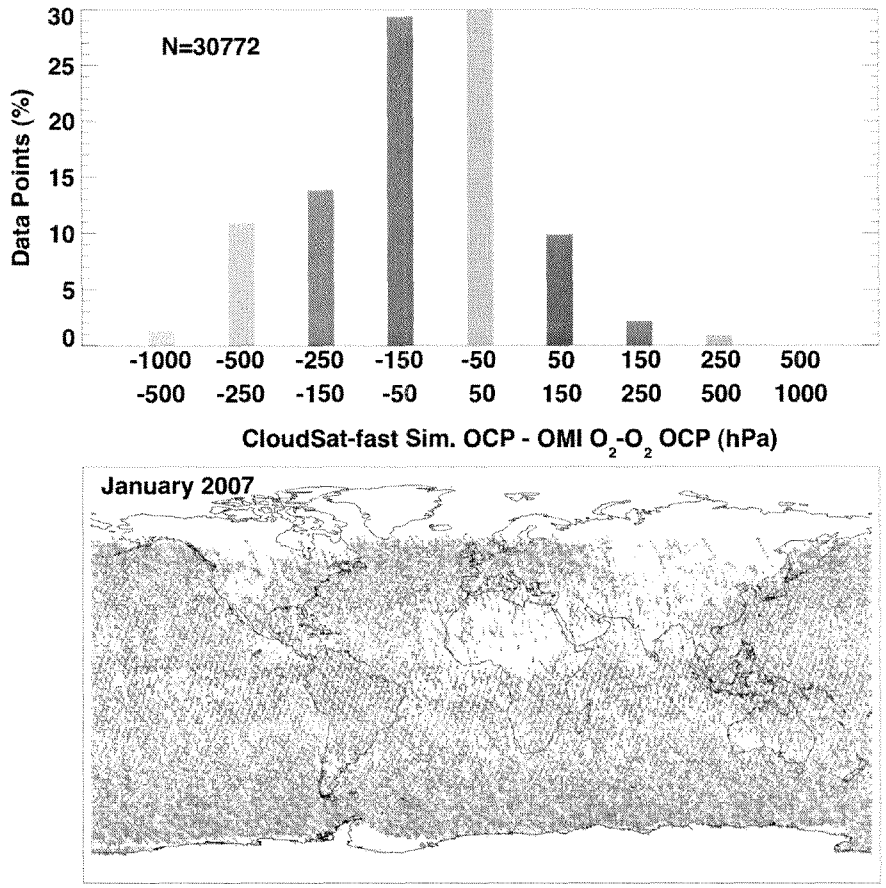


**Fig. 18.** Similar to Fig. 15, but for January 2007.